Article

Analysis of the Complex Three-Dimensional Flow Structure in the Circulation Pump of the Flow-Making System Based on Delayed Detached Eddy Simulation

Zhong Li [1], **Lei Ding** [1], **Weifeng Gong** [2], **Dan Ni** [1,*], **Cunzhi Ma** [1] and **Yanna Sun** [1]

[1]   School of Energy and Power Engineering, Jiangsu University, Zhenjiang 212013, China
[2]   Shanghai Marine Equipment Research Institute (SMERI), Shanghai 200031, China
*   Correspondence: nidan@ujs.edu.cn

Abstract: As the core component of the flow-making system, the circulating pump has differences in its internal flow structure under different operating conditions, which affects the flow quality of the environmental simulation test area and the authenticity of marine environmental simulation. To explore the internal flow characteristics and outlet evolution characteristics of the circulating pump, this paper uses the DDES (delayed detached eddy simulation) method for numerical simulation. This paper combines BVF (boundary vorticity flow) diagnosis and the limit streamline method to analyze the evolution characteristics of the unstable flow area on the blade surface; it uses the Q criterion to identify the vortex structure inside the pump and analyze its evolution and development laws. Additionally, a quantitative analysis of the flow state of the circulating pump using flow uniformity indexes is performed. The results show that the surface of impeller blades is uniform under $1.0\ Q_N$. At $0.7\ Q_N$, the evolution process of the blade suction surface BVF is periodic, with a corresponding period of about 2/9 T (0.02 s). At $1.0\ Q_N$, the strength and scale of the separated vortices inside the guide vanes are minimized compared to other flow rates, and the scale and strength of the vortices show a decreasing trend along the outer normal direction. The evolution period of the separation vortex on the pressure surface of the guide vane is about 1/3 T (0.033 s) under $1.1\ Q_N$ and the evolution period of the suction surface of the guide vane is about 2/3 T (0.067 s) under $0.7\ Q_N$. The flow uniformity indexes value downstream of the pump outlet under $1.0\ Q_N$ are very close to the ideal value; with a corresponding value of $C_i = 0.023$, $\bar{\theta} = 89.94°$, $\gamma = 0.95$, $\lambda = 97.9\%$, the outflow can be approximately regarded as axial uniform flow. The research results can provide theoretical support for the further optimization design of circulating pumps and lay the foundation for the implementation of real systems.

Keywords: flow-making system; circulating pump; internal flow characteristics; BVF; flow uniformity indexes

1. Introduction

The ocean is the focus of current and future human attention. Global ocean development is continuously moving from nearshore to deep sea and ultra-deep sea, becoming a new trend in the competition among ocean powers [1,2]. The circulation flow-making system, as the core facility for improving deep-sea engineering technology, provides an effective platform for various complex environmental conditions in ocean engineering experiments and research, and can accurately measure key information such as speed, pressure, radiation noise, and vibration in the environment simulation area [3]. The axial flow circulation pump is the core hydraulic component that drives the circulation of the fluid medium inside the circulation flow-making system. The control of the outflow quality of the circulation pump is the key to achieving the technical indicators of the circulation flow system to simulate the real ocean environment. The study of the non-steady flow

characteristics inside the circulation pump is an important prerequisite and foundation for achieving effective control of the outflow quality of the circulation pump [4,5].

The internal flow of an axial flow pump during operation is a complex three-dimensional unsteady flow, often resulting in complex flow phenomena and inducing strong pressure pulsations and vibration noise [6]. The study of the internal flow characteristics of axial flow pumps under different parameter conditions is a prerequisite for suppressing the level of pulsation and vibration noise inside the pump [7,8]. Currently, computational fluid dynamics is a powerful method for analyzing the detailed flow field structure inside a water pump; when combined with experimental methods, it can be used to study the complex flow patterns inside an axial flow pump device. Many scholars have conducted extensive research on the three-dimensional flow field and pressure pulsations inside axial flow pump devices. Zuo et al. [9] explored the influence of different rotational speeds on the transient internal and external flow characteristics of axial flow pumps by combining numerical simulations and experiments. AI-Obaidi et al. [10] analyzed the static pressure, axial, tangential, and radial velocity vectors, as well as pressure pulsations inside an axial flow pump, based on the k-epsilon turbulence model and sliding mesh technology. Wang et al. [11] combined numerical simulations and experimental verification to reveal the development process of the skewed flow characteristics inside the S-shaped channel of a 15-degree slanted axial flow pump. Kim et al. [12] found that the steady and unsteady performance characteristics of a submersible axial flow pump depend on the inlet guide vanes (IGV) and blade pitch angle. Zhou et al. [13] improved the internal flow characteristics of an axial flow pump under low flow conditions by adopting a double-inlet structure and combining numerical simulations with experimental methods. Mu et al. [14] proposed a new groove flow control technology for axial flow pumps and used numerical simulation methods to study its internal flow characteristics and improvement effects under stall conditions. Kang et al. [15] found that increasing the number of guide vanes can help improve the uniformity of the axial velocity at the impeller outlet by numerical simulation of the internal flow field of an axial flow pump. Xie et al. [16] studied the significance of the pressure pulsation characteristics inside a prototype pump and a model pump through computational fluid dynamics and experiments and found that numerical simulation predictions can replace model test pressure pulsations. Zhang et al. [17] studied the transient turbulent characteristics and fluid–structure interaction (FSI) characteristics of a vertical axial flow pump under design conditions, and revealed the time-frequency rules of fluid pressure pulsations and structural vibrations at the same position inside the axial flow pump. Yang et al. [18,19] studied the internal flow characteristics and pressure pulsation characteristics inside the impeller and guide vanes of a vertical axial flow pump at different flow rates, and analyzed the internal flow characteristics at the inlet and outlet under different deflection angles based on the k-omega model, finding that the uniformity of the outlet flow velocity and the pressure pulsation are periodic with the increase in the deflection angle. Kan et al. [20] used the k-omega turbulence model to numerically calculate a helical axial flow pump and revealed the influence of the clearance between the blade tip and the casing on the internal flow characteristics by analyzing the pump's pressure, streamline, and turbulent kinetic energy. Feng et al. [21] used numerical methods to study the influence of the clearance between the blade tip and the casing on the pressure fluctuation of an axial flow pump, and proposed a new method based on pressure statistics to determine the pressure fluctuation of all grid nodes in the pump.

There exist complex vortex structures inside an axial flow pump, and these vortices are also an important factor causing pressure pulsations inside the pump, which have garnered significant attention within the domain of academic discourse [22]. Zhao et al. [23] quantitatively analyzed the characteristics of corner vortices in the separated flow of axial flow pumps and found that the average vortex strength and turbulent vortex dissipation gradually weaken along the vortex core line from the corner area to the vortex tail under different operating conditions. Zhang et al. [24] qualitatively and quantitatively analyzed the effect of inlet vortex flow on the performance of a pump device under different inlet

flow conditions through numerical calculations and experiments, and revealed the trend of changes in the internal vortex type of the impeller and the pressure pulsation caused by the vortex. Kan et al. [25] used CFD technology to study the steady-state flow structure and unsteady flow characteristics of an axial flow pump under stall conditions, revealing the mechanism of low-frequency pressure pulsations under stall conditions, and also analyzed the position and evolution of the core area of the guide vane vortex structure under deep stall conditions. Song et al. [26] studied the influence of attached vortices on pressure pulsations in a pump sump by combining experiments and vortex dynamics and found that the pressure pulsation induced by the attached vortices fluctuates periodically with time, and the pressure pulsation curve is approximately a cosine curve. Wu et al. [27] used PIV flow field testing technology to obtain the non-steady-state characteristics of the leakage vortex at the blade tip clearance of an axial flow pump under rated conditions, and analyzed the generation, separation, and fragmentation process of the leakage vortex.

Based on the extensive research results mentioned above, the study of flow characteristics inside axial flow pumps mainly focuses on the pressure pulsation characteristics and typical vortex flow characteristics in the impeller and guide vane interference region. However, compared to that, research on the evolution of multi-scale vortex flow at the pump outlet and downstream is relatively lacking, and the impact of the internal flow on the downstream is yet to be revealed. Therefore, targeted research is urgently needed. In this paper, the DDES method is used to numerically simulate the three-dimensional unsteady flow structure of a circulation pump under different flow rates, and the evolution characteristics of the unstable flow region on the blade surface, the evolution and development laws of the internal vortex structure, and the quantitative analysis of the pump outlet flow state using flow uniformity indicators are analyzed in detail. This lays a model foundation for the smooth implementation of the physical implementation of the circulation system.

## 2. Numerical Simulation and Test Loop

2.1. Model Pump

Considering the existing model test conditions and experimental costs, this paper reduces the scale of the circulation pump in the prototype nominal diameter 6000 mm flow-making system, with a scale ratio of 1:10. According to the theory of fluid machinery similarity, it is possible to predict the relevant unsteady performance of the prototype pump based on the research results of the model pump. The parameters of prototype and model circulating pumps are shown in Tables 1 and 2, and the hydraulic components consist of the front guide vane, impeller, and guide vane, as shown in the three-dimensional structure in Figure 1.

Table 1. The basic design parameters of prototype pump.

Parameter	Value
Flow rate Q_N	460,800 m^3/h
Pump head H_N	2.8 m
Rotational speed n	60 r/min
Specific speed n_s	1145
Impeller blade number Z_i	7
Tip clearance	6 mm
Guide vane blade number Z_g	9
Front guide vane blade number Z_f	4
Impeller inlet diameter D_1	6000 mm
Impeller outlet diameter D_2	6000 mm

Table 2. The basic design parameters of model circulation pump.

Parameter	Value
Flow rate Q_N	4608 m^3/h
Pump head H_N	2.8 m
Rotational speed n	600 r/min
Specific speed n_s	1145
Impeller blade number Z_i	7
Tip clearance	0.6 mm
Guide vane blade number Z_g	9
Front guide vane blade number Z_f	4
Impeller inlet diameter D_1	600 mm
Impeller outlet diameter D_2	600 mm
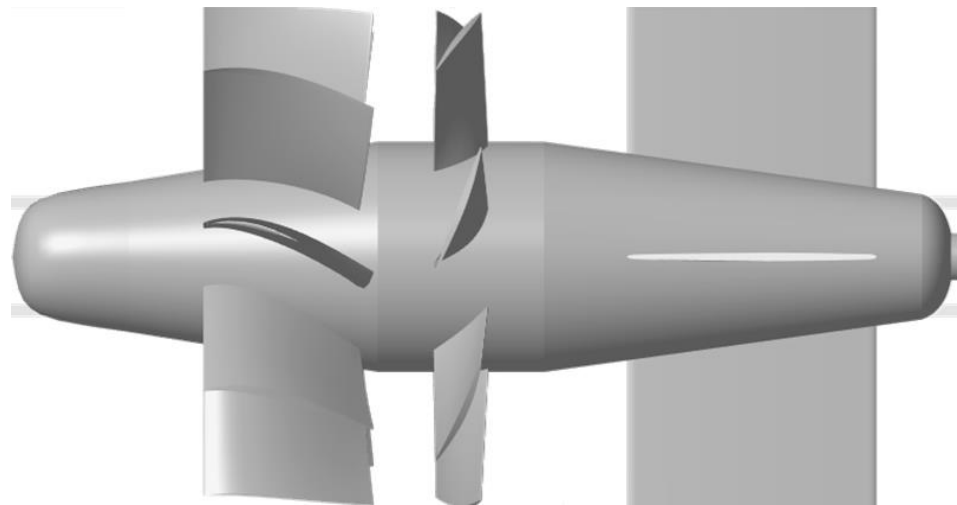
Figure 1. Hydraulic parts of circulating pump.

2.2. Turbulence Model and Boundary Conditions

ANSYS-FLUENT is used to solve the three-dimensional unsteady flow field of the circulating pump. In this study, the SIMPLEC algorithm is used to achieve the coupling between velocity and pressure. The steady-state numerical calculation uses the SST k-ω turbulence model, and the results of the steady-state calculation are used as the initial value for the unsteady-state calculation. The SST k-ω turbulence model inherits the advantages of the traditional k-ω and k-ε model, and can better handle the flow conditions near the wall and in the fully developed flow area. The DDES method avoids the problem of the modeled stress loss in DES and captures the internal flow structure more accurately by introducing a delay function to reconstruct the DES length scale while considering the grid scale and vortex viscosity field [28,29]. Therefore, the DDES method is used in the unsteady numerical calculation.

The DDES turbulent transport equation based on the SST k-ω model is:

$$\frac{\partial(\rho k)}{\partial t} + \frac{\partial(\rho k u_i)}{\partial x_i} = \frac{\partial}{\partial x}\left[\left(\mu + \frac{\mu_t}{\sigma_{k3}}\right)\frac{\partial k}{\partial x_j}\right] + P_k - \rho k^{3/2}/l_{DDES} \tag{1}$$

$$\frac{\partial(\rho\omega)}{\partial t} + \frac{\partial(\rho\omega u_i)}{\partial x_i} = \frac{\partial}{\partial x_j}\left[\left(\mu + \frac{\mu_t}{\sigma_{\omega3}}\right)\frac{\partial\omega}{\partial x_j}\right] + \alpha_3\frac{\omega}{k}P_k - \beta_3\rho\omega^2$$
$$+ 2(1-F_1)\rho\frac{1}{\omega\sigma_{\omega2}}\frac{\partial k}{\partial x_j}\frac{\partial\omega}{\partial x_j} \tag{2}$$

$$\mu_t = \rho\frac{a_1 k}{\max(a_1\omega, SF_2)} \tag{3}$$

where the mixed functions F_1 and F_2 of the SST k-ω model can be represented as

$$F_1 = \tanh(\xi^4) \tag{4}$$

$$\xi = \min\left[\max\left(\frac{\sqrt{k}}{\beta^* \omega d_\omega}, \frac{500\mu}{\rho d_\omega^2 \omega}\right), \frac{4\rho k}{D_\omega^+ \sigma_{\omega 2} d_\omega^2}\right] \tag{5}$$

$$D_\omega^+ = \max\left[2\rho \frac{1}{\sigma_{\omega 2}} \frac{1}{\omega} \frac{\partial k}{\partial x_j} \frac{\partial \omega}{\partial x_j}, 10^{-10}\right] \tag{6}$$

$$F_2 = \tanh\left(\eta^2\right) \tag{7}$$

$$\eta = \max\left\{\frac{2k^{1/2}}{\beta^* \omega d_\omega}, \frac{500\mu}{\rho d_\omega^2 \omega}\right\} \tag{8}$$

where d_ω is the distance from the calculation point to the wall surface; P_k is the turbulence generation term caused by viscous forces, defined the same as the DES model; $\alpha_1 = 5/9$, $\beta_1 = 0.075$, $k_1 = 1.176$, $\sigma_{\omega 1} = 2$, $\alpha_2 = 0.44$, $\beta_2 = 0.0828$, $\sigma_{k2} = 1$, $\sigma_{\omega 2} = 1/0.856$, $a_1 = 0.31$, $\beta^* = 0.09$.

$$l_{DDES} = l_{RANS} - f_d \max(0, l_{RANS} - l_{LES}) \tag{9}$$

$$l_{RANS} = \frac{k^{1/2}}{\beta^* \omega} \tag{10}$$

$$l_{LES} = C_{DES} \Delta \tag{11}$$

$$C_{DES} = F_1 C_{DES1} + (1 - F_1) C_{DES2} \tag{12}$$

$$\Delta = \max\{\Delta x, \Delta y, \Delta z\} \tag{13}$$

$$f_d = 1 - \tanh\left[\left(C_{d1} r_d\right)^{C_{d2}}\right] \tag{14}$$

$$r_d = \frac{v_t + v}{\sqrt{\frac{1}{2}(S^2 + \Omega^2) k^2 d_\omega^2}} \tag{15}$$

where f_d is the delay function; r_d is the delay factor; S is the value of the strain rate tensor; Ω is the value of the curl tensor; Δ is the maximum side length of the unit; Constant $k = 0.41$, $C_{DES1} = 0.78$, $C_{DES2} = 0.61$, $C_{d1} = 8$, $C_{d2} = 3$.

The equations and the constants in the equations could be found in the published paper [30].

The inlet boundary condition is velocity inlet with parameters calculated from the experimental conditions, and the outlet boundary condition is pressure outlet with a value set to a standard atmospheric pressure. All physical wall surfaces use a no-slip wall condition. The specific turbulence characteristics with a turbulence intensity of 5% are given. The calculation convergence residual is set to 1×10^{-6}.

2.3. Mesh Generation

The calculation domain of the circulation pump consists of the inlet section, rectangular diffuser section, front guide vane, impeller, guide vane, and outlet section, as shown in Figure 2a. To improve the reliability of numerical simulation, the length of the inlet and outlet sections is extended by 3 times the pipe diameter length, while the tip clearance is consistent with the experiment, which is 1‰ of the impeller outer diameter. Structured grids have higher accuracy and better convergence in numerical simulation. Therefore, the

hexahedral structure grid in ANSYE-ICEM is used in this paper to partition the calculation domain of the circulation pump. In addition, due to the significant reverse pressure gradient near the blade surface, flow separation is prone to occur. To reproduce the flow characteristics more realistically, an O-type grid and block rotation technology are used to construct the topological structure of the blade surface and local refinement is performed, where the height of the first layer of the blade surface is 0.01 mm, as shown in Figure 2b. A small $Y+$ value is required in the impeller to obtain better flow structure. The average $Y+$ value of the blade surface is calculated and analyzed to be less than 4, which meets the requirements of the DDES numerical calculation. The distribution of the $Y+$ values on the blade surface is shown in Figure 2c.


(**a**)

(**b**)

(**c**)
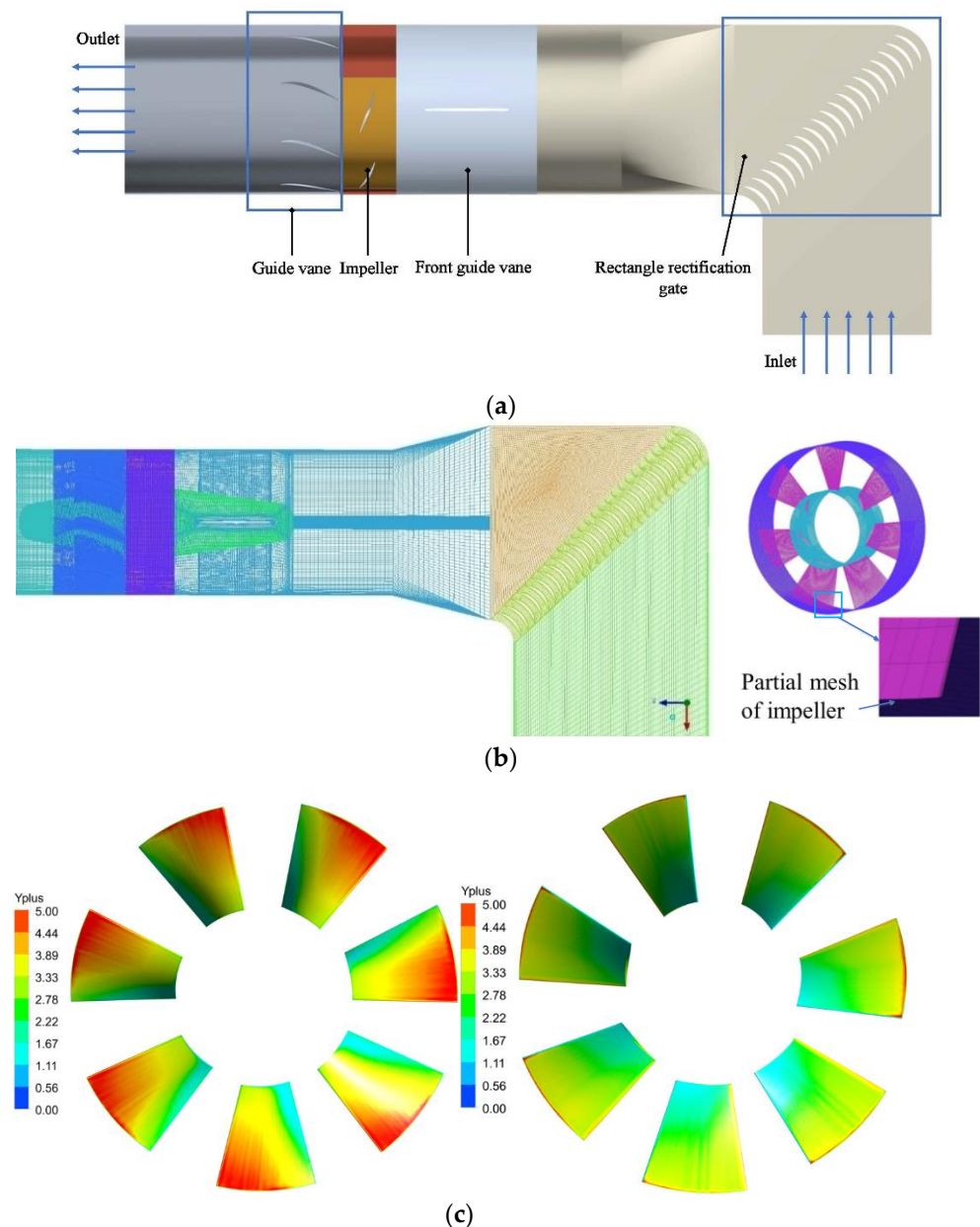
Figure 2. Computational domain structured grid. (**a**) Computational domain of circulating pump. (**b**) Structured mesh of circulating pump and partial mesh of impeller. (**c**) $Y+$ distribution on blades.

Based on whether the head obtained from the unsteady calculation tends to be stable with the total number of grids, an independence verification of the calculation domain grid is carried out. Five grid division schemes are designed, as shown in Table 3.

**Table 3.** Different mesh numbers' division schemes.

Grid Division Schemes	Impeller	Guide Vane	Total Number of Grids
1	1,656,789	1,545,652	4,654,234
2	1,865,448	1,845,487	5,454,876
3	2,254,665	2,044,548	6,546,445
4	3,331,710	2,849,253	9,850,983
5	4,125,842	3,045,456	11,456,687

As shown in Figure 3, when the total number of grids exceeds 11,456,687, the head of the circulation pump changes slightly with the total number of grids. Considering the accuracy and economy of numerical calculation, grid division scheme 5 is selected, where the total grid quality is greater than 0.4.
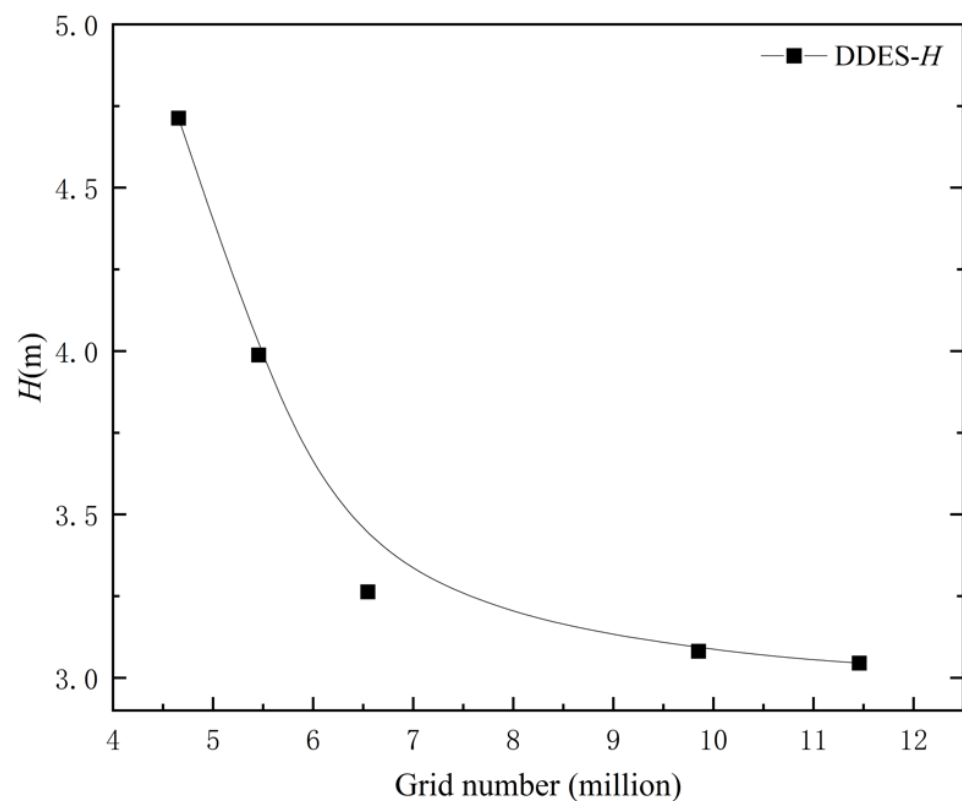
Figure 3. Mesh sensitivity check.

2.4. Test Loop

An experimental system is built to verify the reliability of the numerical simulation method, as shown in Figure 4. The regulation of the operating conditions of the circulating pump is achieved by adjusting the opening of the outlet butterfly valve in the system. The flow rate is collected using an electromagnetic flowmeter (KROHNE, accuracy ± 0.3%). The static pressure at the pump inlet and outlet is collected by a pressure transmitter (EJA, accuracy ± 0.075%). The shaft power and rotational speed are measured using the electrical power measurement method (accuracy ± 0.5%, shaft power analyzed using the loss analysis method). The instruments and motors are connected to the measurement and control center, where data are automatically collected, analyzed, and precise adjustment of the operating conditions is performed. The hydraulic performance of the circulation pump is obtained by collecting parameters in the full operating range of the circulation pump.
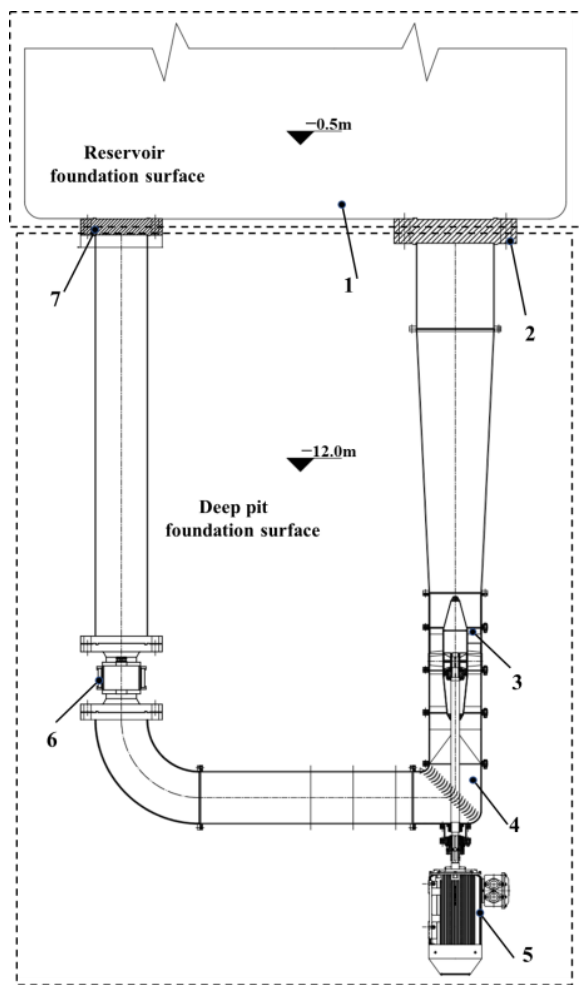
Figure 4. Test loop includes: 1. Reservoir; 2. Outlet butterfly valve; 3. Prototype pump; 4. Rectangular rectifier gate; 5. Low noise motor; 6. Electromagnetic flowmeter; 7. Inlet butterfly valve. (**a**) Top view of the test loop. (**b**) Actual photo of the test loop.

3. Experimental Validation

The average transient parameters of the last five cycles obtained from unsteady numerical calculation are compared and analyzed with the experimental measurement results, and the results are shown in Figure 5. The figure shows that the optimal flow rate obtained from the numerical calculation is consistent with the experimental measurement. The error between the pump head obtained from the numerical calculation and the experimental measurement at 1.0 Q_N is only 3.4%. The maximum error between the two heads in the range of 0.6 Q_N to 1.1 Q_N is only 6%. The trend of the results obtained from the numerical calculation and the experimental measurement also has good consistency under other flow rates. The critical stall and deep stall points are basically the same, indicating that the numerical calculation method used in this paper has a high calculation accuracy.
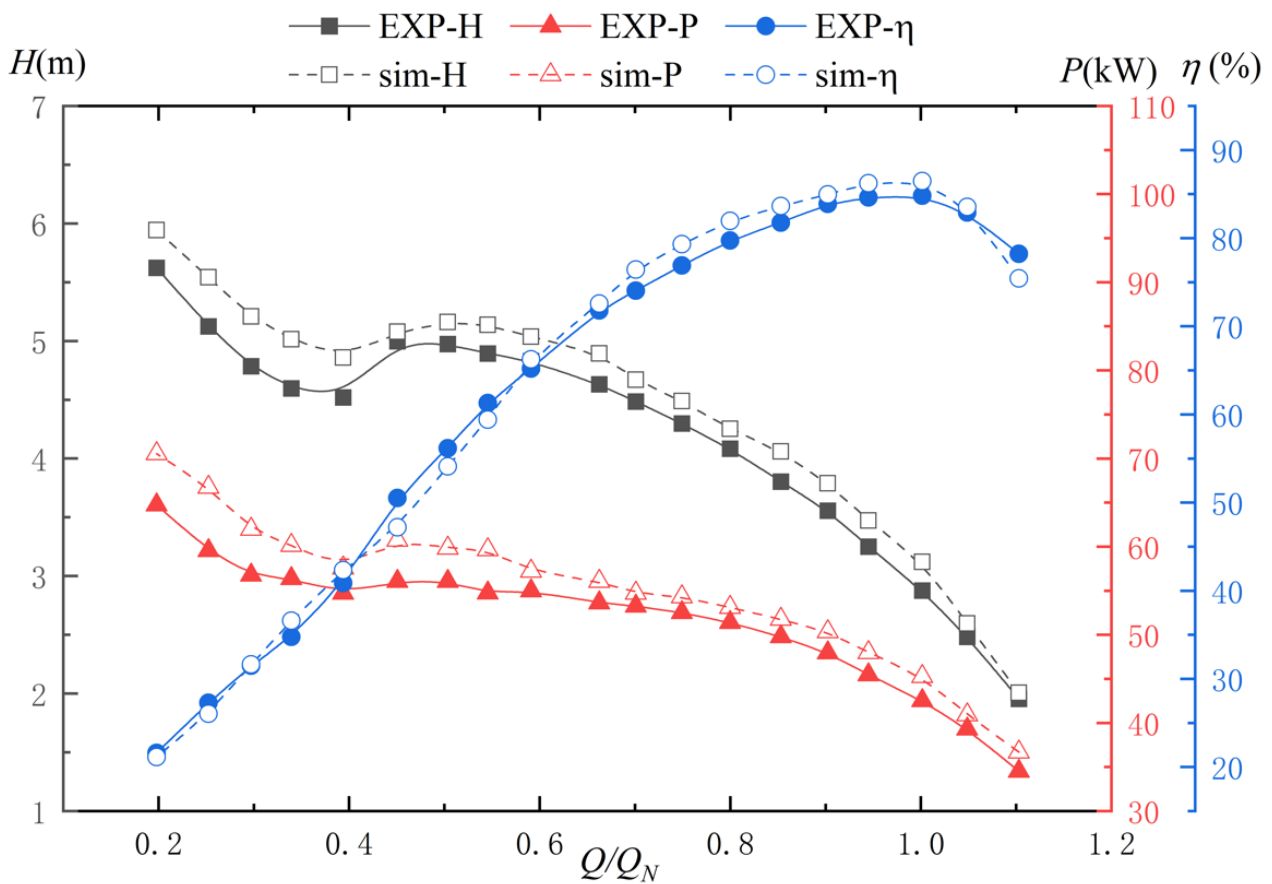
Figure 5. Comparison between experimental and numerical result of circulating pump.

4. Result

4.1. Blade Surface Flow Analysis

Boundary vorticity flow (BVF) is the root cause of the generation and diffusion of vorticity in the impeller of an axial flow pump. The BVF-based flow diagnosis can effectively capture the root cause of bad flow in turbomachinery. By using the BVF diagnostic method, the local key information on the blade surface will be easily identified. Therefore, the BVF diagnostic method is used to analyze the complex flow structure on the surface of the circulating pump blade under different flow rates and to analyze the positive and negative contribution areas of the blade torque through the BVF distribution results on the blade surface.

BVF refers to the vortex flux entering a unit area of fluid per unit time [31,32], and its dynamic description is as follows:

$$\sigma = \sigma_a + \sigma_p + \sigma_\tau \tag{16}$$

$$\sigma_a = n \times a_B \tag{17}$$

$$\sigma_p = \frac{1}{\rho} n \times \nabla \pi \tag{18}$$

$$\sigma_\tau = v(n \times \nabla) \times \omega \tag{19}$$

where σ is the combined value of BVF, and σ_a, σ_p, σ_τ, respectively, refer to the BVF caused by wall acceleration, tangential pressure gradient, and boundary vortices.

During the numerical analysis of the circulating pump, due to the non-sliding wall surface, the large Reynolds number ($\sigma_\tau \ll \sigma_p$) and the compressibility of the fluid, it can

be approximately considered that BVF is mainly generated by the tangential pressure gradient σ_p. The moment is converted into the integral of BVF through derivative moment transformation (DMT), and its calculation formula is as follows:

$$M_z = -\frac{1}{2}\int_{S_b} \rho r^2 \sigma_{pz}\,\mathrm{d}S + \frac{1}{2}\int_{\partial S_b} \rho r^2\,\mathrm{d}Z \tag{20}$$

where M_z is the torque exerted by the fluid on the blade; S_b is the surface area; r is the radius; σ_{pz} is the component of σ_p in the axial direction.

Based on this, combined with the limit streamline method, the flow structure on the blade surface under the flow rates of 0.7 Q_N, 1.0 Q_N, and 1.1 Q_N is analyzed, and the blade surface BVF and limit streamline distribution cloud maps of the impeller blade are shown in Figure 6. At 1.0 Q_N, the flow lines on the blade surface are distributed uniformly, and there is only a weak deviation flow phenomenon at the outlet edge (OE) of the suction surface; in addition, the BVF and flow lines on the pressure surface are uniformly distributed circumferentially. At 1.1 Q_N, the distribution law of BVF and limit streamline is similar to 1.0 Q_N. At 0.7 Q_N, there are obvious BVF peak transition areas on the suction surface inlet hub side, the blade inlet edge (IE) side, and the outlet near the hub side of the impeller blade, and a large area of backflow zone is found near the hub at the outlet combined with the limit streamline; additionally, there is a forward peak point of BVF, which causes unstable flow on the suction surface. There is a negative BVF area on the pressure surface hub side, and a large area of turbulence appears in the limit streamline, which becomes stable as the blade height increases.
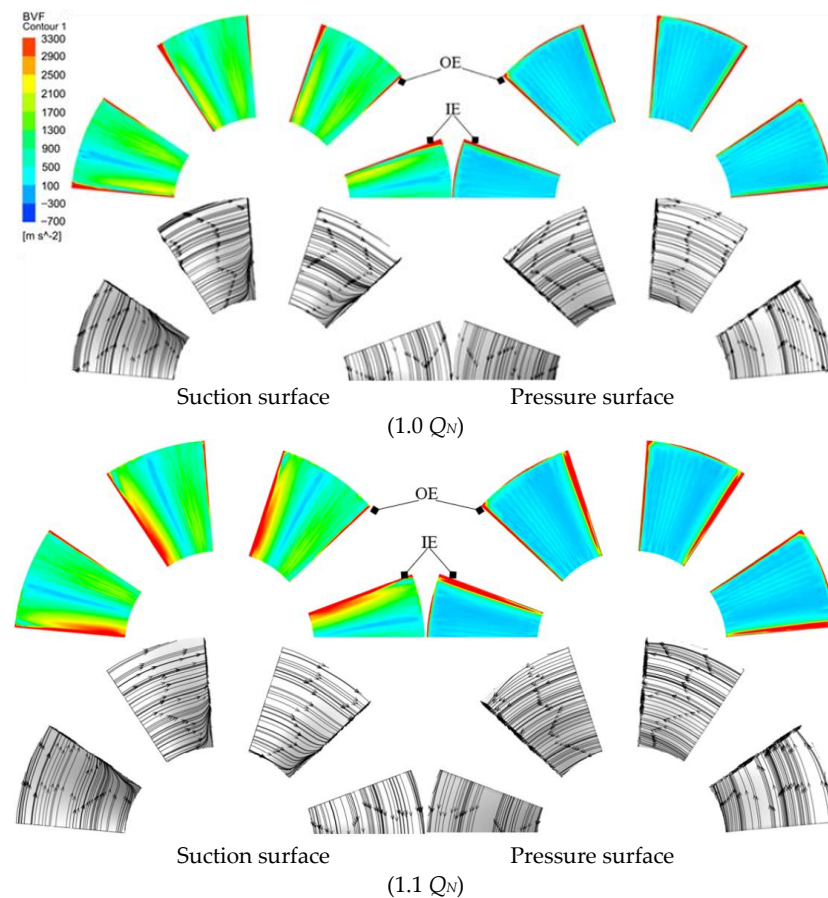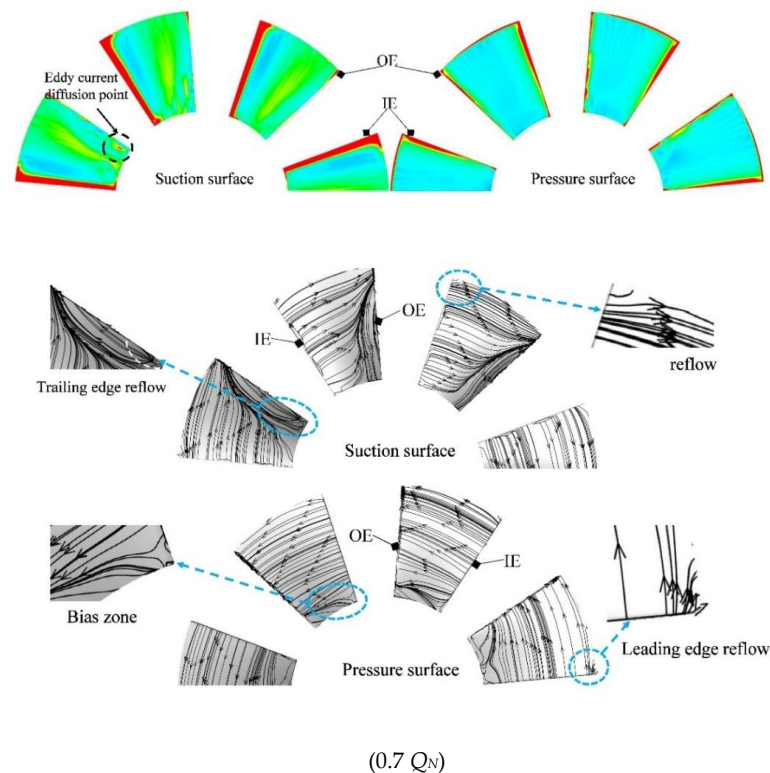

Suction surface　　　　　　　　　Pressure surface

(1.0 Q_N)

Suction surface　　　　　　　　　Pressure surface

(1.1 Q_N)

Figure 6. *Cont.*

(0.7 Q_N)

**Figure 6.** BVF and limit streamline distribution.

To further analyze the evolution of the backflow at the trailing edge of the suction surface and the deviation flow on the pressure surface, the BVF on the suction and pressure surfaces of the blade at different times is analyzed under 0.7 Q_N, and the distribution cloud map is shown in Figure 7. The evolution of the BVF on the suction surface of the blade corresponds to a period of about 2/9T (0.02 s), and the peak BVF area is generated at the inlet hub and continuously evolves and dissipates towards the outlet edge, forming a large range of tilted flow on the suction surface. The BVF distribution cloud map on the pressure surface of the blade shows a trend of alternating positive and negative BVF on the near hub side, and the evolution process has obvious periodicity. Comparing the BVF cloud maps on the suction and pressure surfaces, it is found that the flow stability on the pressure surface is better than that on the suction surface under 0.7 Q_N.

4.2. Internal Vortex Structure

To analyze the evolution process of multi-scale vortices in the circulation pump, the Q criterion is used to identify the vortices in the guide vanes, where Q = 2 × 10^5 s^{-2} is selected as the equivalent surface for vortex identification, and the vortex structure is colored by pressure.

From the hub to the rim, S1, S2, and S3 sections are selected, corresponding to 20%, 50%, and 80% blade height, respectively, as shown in Figure 8. Figure 9 shows the vortex structure and streamline distribution of different radial sections in the guide vane domain under different flow rates. At 1.0 Q_N, the vortex intensity in the guide vane passage is small, and the guide vane wake is more obvious at 20% blade height than at 50% and 80% blade height. Compared with 1.0 Q_N, the separation vortex at the leading edge and trailing edge of the guide vane is enhanced under 1.1 Q_N, and the positive and negative vortices generated on the pressure surface of the guide vane migrate downstream along the near-wall surface and detach at the wake, causing the main flow to deflect. At 0.7 Q_N, the vortex scale and intensity in the guide vane passage and the outflow passage are significantly larger than 1.0 Q_N and 1.1 Q_N. Large-scale vortices are formed inside the guide vane, especially near the hub side, which disrupt the normal flow of the main flow. In

addition, the vortex shedding and dissipation area of the guide vane wake are significantly increased. Combined with the streamline distribution under different operating conditions, the intensity and scale of the internal vortices in the guide vane decrease radially from the hub to the rim.

(**a**)

(**b**)
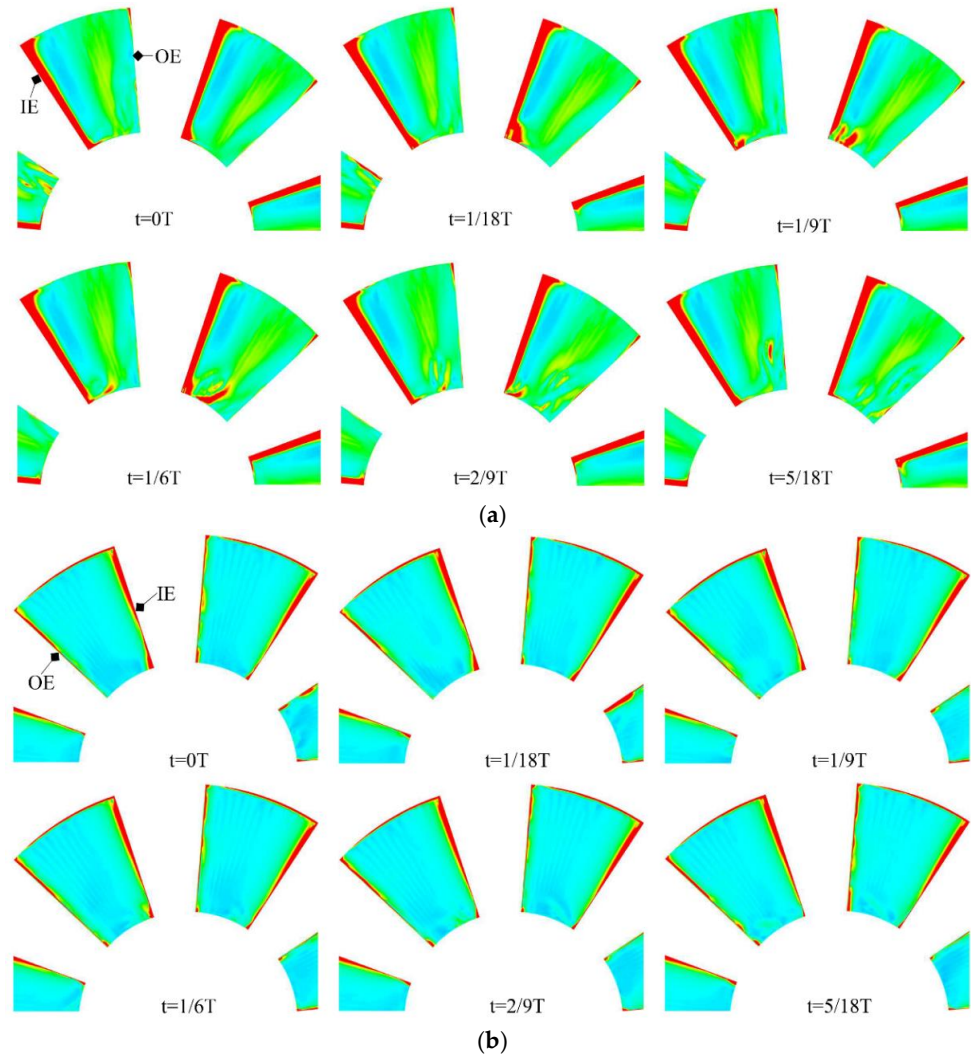
Figure 7. BVF evolution process on blade surface at 0.7 Q_N. (**a**) Suction surface. (**b**) Pressure surface.
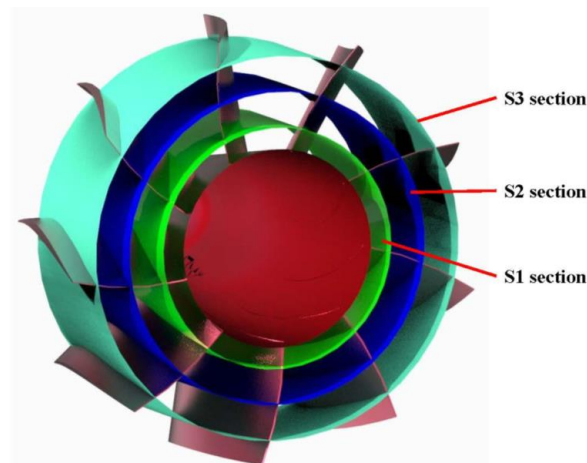
Figure 8. Section diagram of guide vane with different radii.
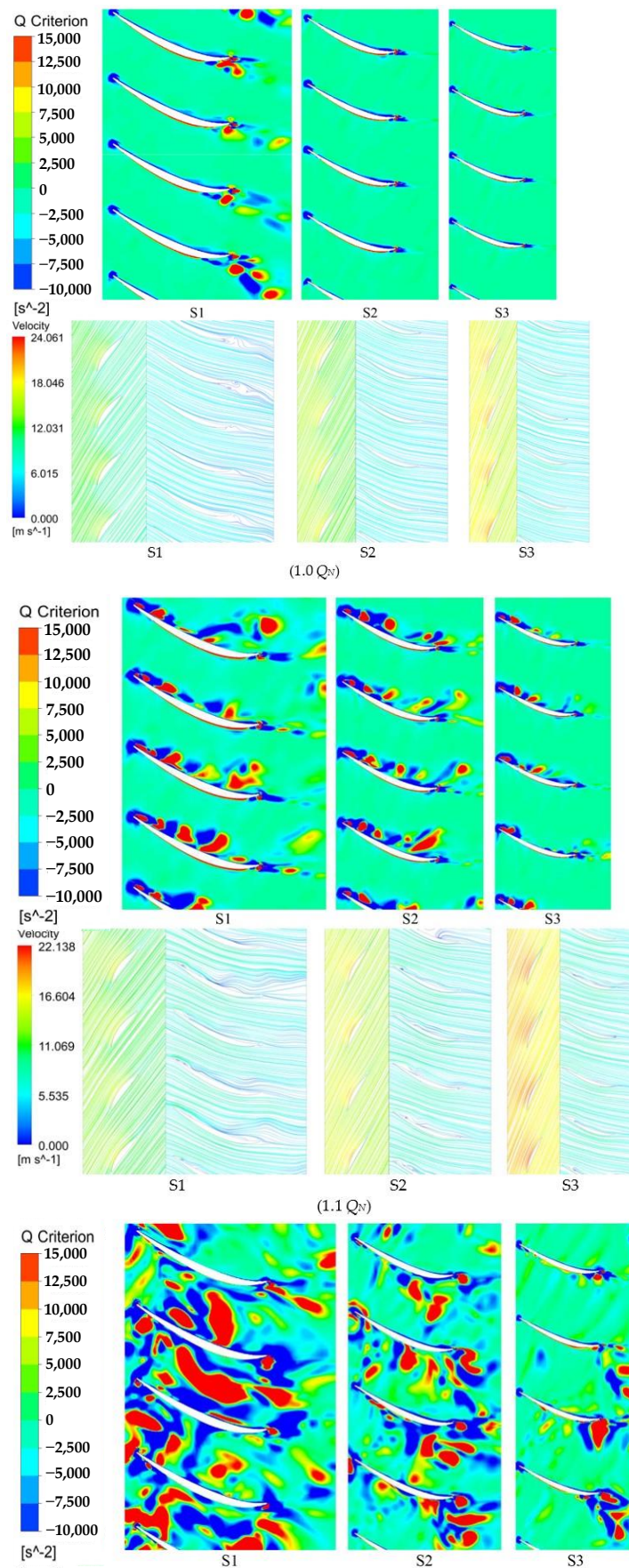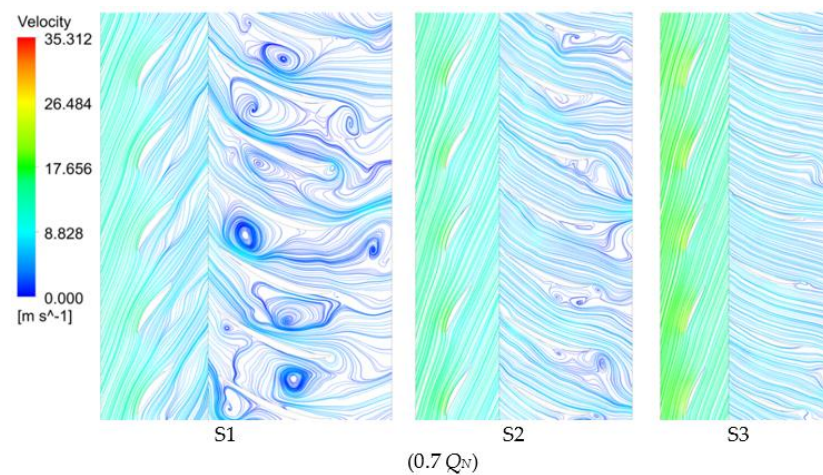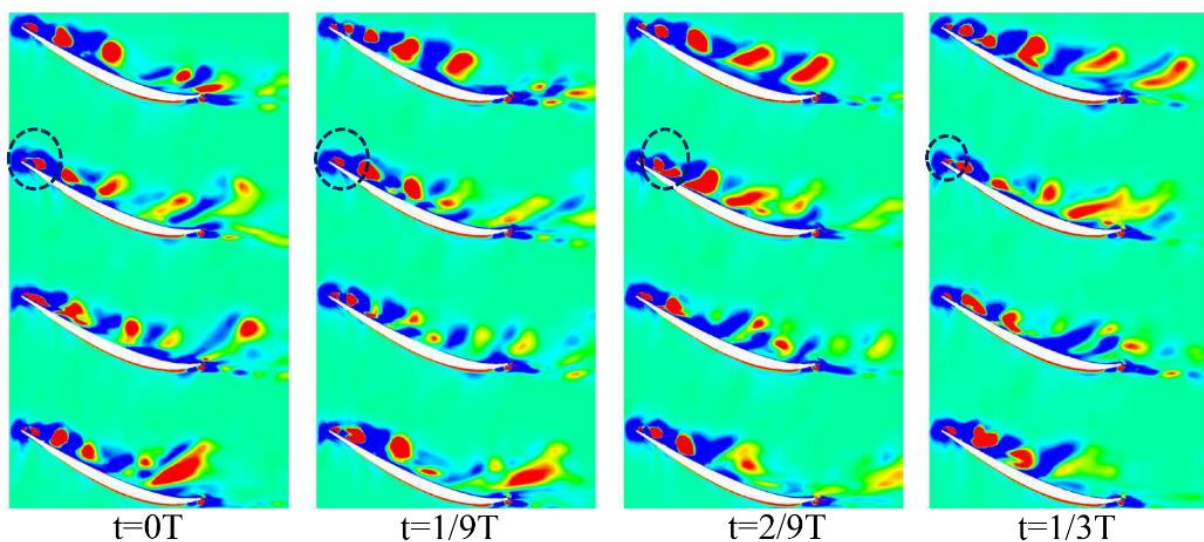
Figure 9. *Cont.*

Figure 9. Distribution of vortex structures and streamline with different span.

The evolution of the vortices inside the circulation pump guide vane is more intense under 1.1 Q_N and 0.7 Q_N. Taking the 50% blade height section as an example for vortex evolution analysis, the evolution process of the vortices at different times is shown in Figure 10. At 1.1 Q_N, the evolution period of the separation vortex generated at the leading edge of the pressure surface of the guide vane is about 1/3T (0.033 s). At 0.7 Q_N, the positive vortex is generated at the leading edge of the suction surface of the guide vane, and then migrates downstream with its scale gradually increasing. When the vortex detaches from the suction surface and enters the main flow passage, it gradually dissipates, and its evolution period is about 2/3T (0.067 s). It can be inferred that multi-scale and different evolution period vortices inside the guide vane under the small flow rate condition will induce complex discrete excitation signals.
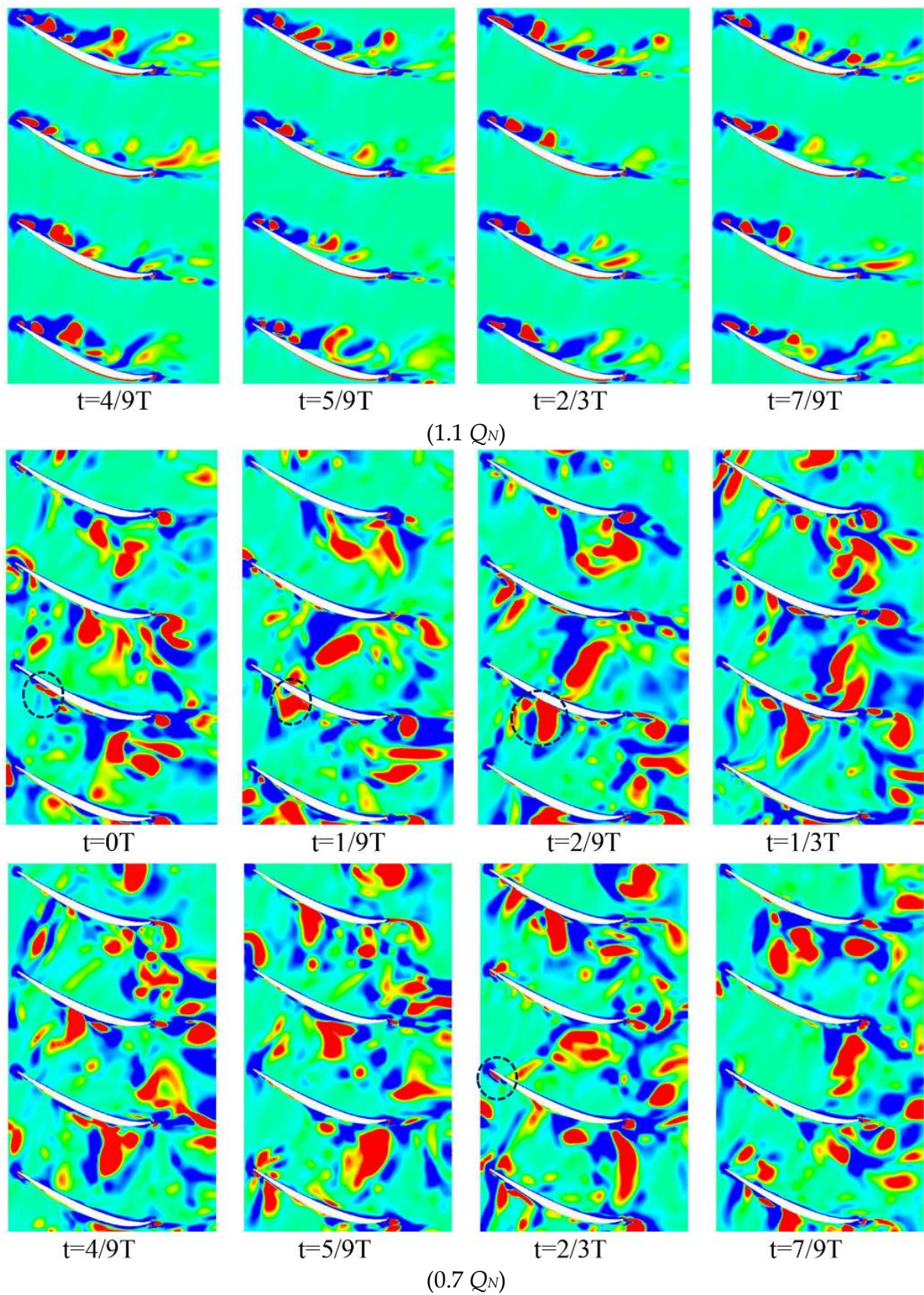

Figure 10. *Cont.*

t=4/9T   t=5/9T   t=2/3T   t=7/9T

(1.1 Q_N)

t=0T   t=1/9T   t=2/9T   t=1/3T

t=4/9T   t=5/9T   t=2/3T   t=7/9T

(0.7 Q_N)

Figure 10. Contour of vortex structure evolution in stator passage.

4.3. Flow Uniformity

Since the environmental simulation test area in the circulation system is located downstream of the circulation pump, the flow uniformity of the pump outlet directly affects the flow quality of the environmental simulation test area. The flow uniformity index is used to compare and analyze the flow uniformity of the pump outlet section (distance from the guide vane outlet is 350 mm, as shown in Figure 11) under different flow rates. The commonly used definition and calculation method of the flow uniformity index are as follows:
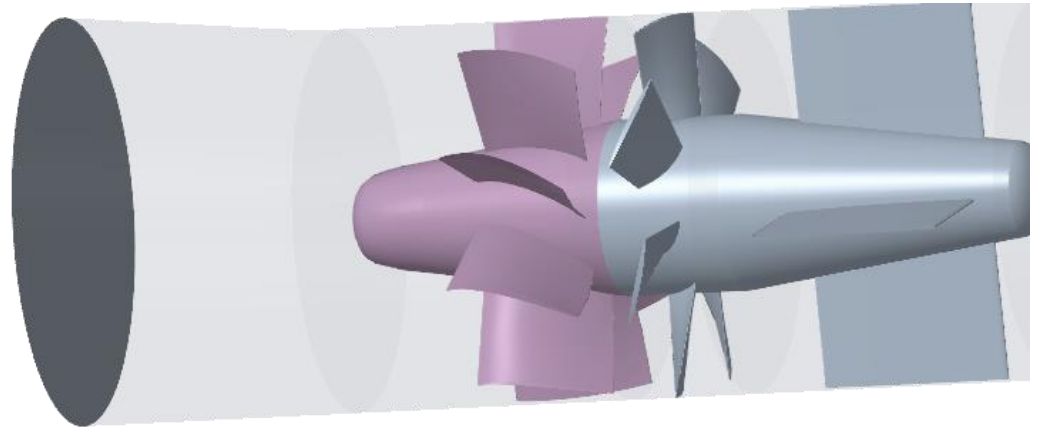
Figure 11. Outflow quality evaluation section.

(1)　Unevenness

The unevenness is the arithmetic mean of the difference between the axial velocity and the average velocity of the flow section [33], and its calculation formula is:

$$\zeta_i = \frac{1}{Q} \int_{A_i} \sqrt{(v_z - \overline{v}_i)^2} dA \tag{21}$$

where Q is the volumetric flow rate, m^3/s; v_z is the axial velocity of the flow section, m/s; A_i is the i-th overcurrent section; $\overline{v}_i$ is the average velocity of the i-th flow section, m/s. Under ideal conditions, the uniform flow corresponds to $\zeta_i = 0$.

(2)　Flow verticality

The flow verticality is the average angle between the axial velocity and tangential velocity of the flow section [24], and its calculation formula is:

$$\overline{\theta} = 90° - \frac{1}{Q} \int_{A_i} v_z \arctan\left(\frac{v_u}{v_z}\right) dA \tag{22}$$

where v_u is the tangential velocity of the flow section, m/s; corresponding to uniform flow in an ideal state $\overline{\theta} = 90°$.

(3)　Speed uniformity index

The velocity uniformity index is defined based on statistical deviation and can reflect the distribution characteristics of fluid velocity in the flow section. It has the advantages of strong comparability and wide applicability [24], and its calculation formula is:

$$\gamma = 1 - \frac{v'}{2\overline{v}} = 1 - \frac{\sum\limits_{i=1}^{n} A_i \sqrt{(v_i - \overline{v})^2}}{2 \sum\limits_{i=1}^{n} A_i v_i} \tag{23}$$

where v_i and $\bar{v}$ is the average velocity of the measuring point and the flow section, m/s. Under ideal conditions, the corresponding $\gamma = 1$ corresponds to uniform flow.

(4)   Uniformity evaluation index based on area weighted average

The uniformity evaluation index based on area weighted average is the relative ratio of area weighted average velocity and quality weighted average velocity. This index is not directly related to the sample points and can quickly evaluate the uniformity of the flow section. It has obvious advantages in evaluating the flow uniformity of the flow section in numerical simulation [34], and its calculation formula is:

$$\lambda = (1 - \frac{|v_a - v_m|}{v_m}) \times 100\% \tag{24}$$

$$v_a = \frac{1}{A} \sum_{j=1}^{n} v_j |A_j| \tag{25}$$

$$v_m = \frac{\sum\limits_{j=1}^{n} v_j \rho_j |v_j \cdot A_j|}{\sum\limits_{j=1}^{n} \rho_j |v_j \cdot A_j|} \tag{26}$$

where v_a and v_m are area weighted average velocity and mass weighted average velocity, respectively; A represents the cross-sectional area of the flow passage; the A_j and v_j sub tables represent the area vector and velocity vector on the j-th unit surface; ρ_j represents the fluid density on j unit surfaces; n is the number of unit surfaces divided by the flow section.

After calculation, the index value of flow uniformity at the pump outlet is shown in Table 4, in which: when $C_i = 0$, $\bar{\theta} = 90°$, $\gamma = 1$, $\lambda = 100\%$, it corresponds to ideal uniform flow.

Table 4. Comparison of evaluation section uniformity indexes.

Q/Q_N	C_i	$\bar{\theta}$ (°)	γ	λ (%)
0.6	0.11	86.3	0.85	90.2
0.7	0.08	88.7	0.88	92.3
0.8	0.04	89.9	0.9	94.5
0.9	0.023	89.94	0.92	96.7
1.0	0.023	89.94	0.95	97.9
1.1	0.04	89.2	0.92	96.5

Each uniformity index has obtained the optimal value under 1.0 Q_N, and its corresponding optimal values are $C_i = 0.023$, $\bar{\theta} = 89.94°$, $\gamma = 0.95$, $\lambda = 97.9\%$, respectively, and its flow state can be approximated as normal uniform outflow. On the whole, the variation trend of each uniformity index with the flow rate is consistent; that is, with the increase in deviation from the rated working condition, the flow uniformity at the pump outlet decreases.

In order to further analyze the distribution characteristics of the circulating pump outflow under 1.0 Q_N, the velocity distribution curves at different radii as shown in Figure 12 are given.

As shown in the above figure, at 1.0 Q_N, the speed uniformity of the hub and rim side of the outlet section of the circulating pump in the circumferential direction is obviously weaker than that in the main passage, the speed fluctuation amplitude at the hub side is the largest, and the speed fluctuation amplitude at the radius of 0.7 r/R is the smallest.
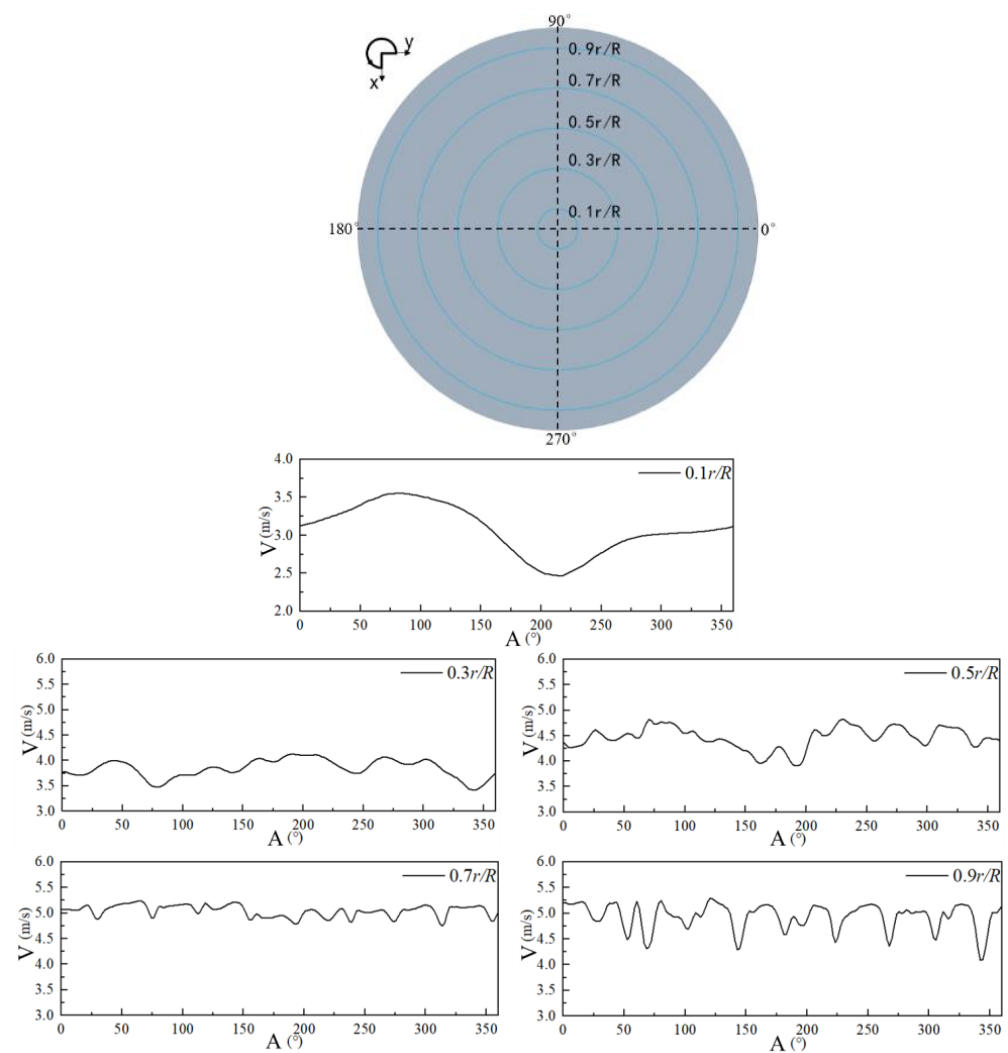
Figure 12. Velocity distribution curves at different radii.

5. Conclusions

This article adopts the DDES method to perform unsteady numerical simulation of the internal flow of the circulating pump under different flow rates. Methods such as the BVF flow diagnosis, limit streamlines, and Q criteria are used to analyze the evolution and development laws of the unstable flow structure in the circulating pump, and to quantitatively evaluate the flow uniformity of the pump outlet. The main conclusions obtained are as follows.

By comparing the energy performance test of the pump with the numerical calculation, the accuracy of the DDES method is verified.

The flow stability on the suction side of the blade is lower than that on the pressure side under different flow rates. At 0.7 Q_N, there is a peak point of BVF on the suction side, which is the main reason for the unstable flow on the suction surface. The turbulence on the pressure surface gradually improves with the increase in the blade height. The evolution period of the BVF on the suction surface of the blade is 0.02 s, and the BVF peak is generated on the inlet hub side and continuously dissipates towards the outlet. The pressure surface of the blade exhibits an alternating trend of positive and negative BVF evolution.

Under off-design flow rates, the internal flow of the guide vane exhibits strong unsteady characteristics. The intensity and scale of the vortex structure in the guide vane flow passage weaken from the hub to the rim under different flow rates. At 0.7 Q_N, the suction surface vortex migrates downstream, and its scale gradually increases before detachment and dissipation. At 1.1 Q_N, the forward vortex evolves along the pressure surface of the

guide vane. The evolution period of the vortex structure varies under different flow rates, with approximately 0.033 s for 0.7 Q_N and approximately 0.067 s for 1.1 Q_N. The multi-scale and different period vortex evolution inside the guide vane under 0.7 Q_N is the main cause of complex discrete signals.

The outlet position of the circulating pump is validated based on the internal flow and flow uniformity index. The analysis shows that the flow uniformity index of the circulating pump achieves optimal values under 1.0 Q_N, and the fluctuation amplitude of velocity gradually decreases with the increase in the blade height.

Author Contributions: Methodology, D.N.; validation, Z.L.; investigation, L.D.; resources, W.G.; data curation, C.M.; supervision, Y.S. All authors have read and agreed to the published version of the manuscript.

Data Availability Statement: Not applicable.

Conflicts of Interest: The authors declare no conflict of interest in the paper.

Abbreviations

Acronyms	
CFD	Computational Fluid Dynamics
DDES	Delayed Detached Eddy Simulation
DES	Detached Eddy Simulation
BVF	Boundary Vorticity Flow
DMT	Derivative Moment Transformation
Symbols	
Q_N	Flow rate
H_N	Pump head
n	Rotational speed
n_s	Specific speed
D_1	Impeller inlet diameter
D_2	Impeller outlet diameter
Z_i	Impeller blade number
Z_g	Guide vane blade number
Z_f	Front guide vane blade number
ς	Unevenness
$\bar{\theta}$	Flow verticality
γ	Speed uniformity index
λ	Uniformity evaluation index based on area weighted average

References

1. Hein, J.R.; Koschinsky, A.; Kuhn, T. Deep-ocean polymetallic nodules as a resource for critical materials. *Nat. Rev. Earth. Environ.* **2020**, *1*, 158–169. [CrossRef]
2. Jouffray, J.B.; Blasiak, R.; Norstrom, A.V.; Osterblom, H.; Nystrom, M. The Blue Acceleration: The Trajectory of Human Expansion into the Ocean. *One Earth* **2020**, *2*, 43–54. [CrossRef]
3. Li, H.J.; Liu, Y.; Liang, B.C.; Liu, F.S.; Wu, G.X.; Du, J.F.; Hou, H.M.; Li, A.J.; Shi, L.M. Demands and challenges for construction of marine infrastructures in China. *Front. Struct. Civ. Eng.* **2022**, *16*, 551–563. [CrossRef]
4. Zhang, X.W.; Tang, F.P. Investigation on hydrodynamic characteristics of coastal axial flow pump system model under full working condition of forward rotation based on experiment and CFD method. *Ocean. Eng.* **2022**, *253*, 111286. [CrossRef]
5. Li, W.Y.; Zhang, X.Y.; Shuai, Z.J.; Jiang, C.X.; Li, F.C. CFD Numerical Simulation of the Complex Turbulent Flow Field in an Axial-Flow Water Pump. *Adv. Mech. Eng.* **2014**, 521706. [CrossRef]

6. Chen, E.Y.; Ma, Z.L.; Zhao, G.P.; Li, G.P.; Yang, A.L.; Nan, G.F. Numerical investigation on vibration and noise induced by unsteady flow in an axial-flow pump. *J. Mech. Sci. Technol.* **2016**, *30*, 5397–5404. [CrossRef]
7. Duan, X.H.; Tang, F.P.; Duan, W.Y.; Zhou, W.; Shi, L.J. Experimental investigation on the correlation of pressure pulsation and vibration of axial flow pump. *Adv. Mech. Eng.* **2019**, *11*, 1687814019889473. [CrossRef]
8. Yang, F.; Jiang, D.J.; Yuan, Y.; Lv, Y.T.; Jian, H.F.; Gao, H. Influence of Rotation Speed on Flow Field and Hydraulic Noise in the Conduit of a Vertical Axial-Flow Pump under Low Flow Rate Condition. *Machines* **2022**, *10*, 691. [CrossRef]
9. Zuo, Z.L.; Tan, L.W.; Shi, W.D.; Chen, C.; Ye, J.C.; Francis, E.M. Transient Characteristic Analysis of Variable Frequency Speed Regulation of Axial Flow Pump. *Sustainability* **2022**, *14*, 11143. [CrossRef]
10. Al-Obaidi, A.R.; Mohammed, A.A. Numerical Investigations of Transient Flow Characteristic in Axial Flow Pump and Pressure Fluctuation Analysis Based on the CFD Technique. *J. Eng. Sci. Technol. Rev.* **2019**, *12*, 70–79. [CrossRef]
11. Wang, C.Y.; Wang, F.J.; Tang, Y.; Zi, D.; Xie, L.H.; He, C.L.; Zhu, Q.R.; Huang, C.B. Investigation Into the Phenomenon of Flow Deviation in the S-Shaped Discharge Passage of a Slanted Axial-Flow Pumping System. *J. Fluid. Eng-T Asme.* **2020**, *142*, 041205. [CrossRef]
12. Kim, Y.S.; Shim, H.S.; Kim, K.Y. Effects of inlet guide vane and blade pitch angles on the performance of a submersible axial-flow pump. Proc. *Inst. Mech. Eng. Part A J. Power Energy* **2021**, *235*, 718–732. [CrossRef]
13. Zhou, Y.S.; Zhang, H.; Chen, B. Influence of double-inlet design on the flow-head characteristics of axial-flow pump. *J. Hydrodyn.* **2021**, *33*, 763–772. [CrossRef]
14. Mu, T.; Zhang, R.; Xu, H.; Zheng, Y.; Fei, Z.D.; Li, J.H. Study on improvement of hydraulic performance and internal flow pattern of the axial flow pump by groove flow control technology. *Renew. Energ.* **2020**, *160*, 756–769. [CrossRef]
15. Kang, C.; Yu, X.J.; Gong, W.F.; Li, C.J.; Huang, Q.F. Influence of stator vane number on performance of the axial-flow pump. *J. Mech. Sci. Technol.* **2015**, *29*, 2025–2034. [CrossRef]
16. Xie, C.L.; Tang, F.P.; Zhang, R.T.; Zhou, W.; Zhang, W.P.; Yang, F. Numerical calculation of axial-flow pump's pressure fluctuation and model test analysis. *Adv. Mech. Eng.* **2018**, *10*, 1687814018769775. [CrossRef]
17. Zhang, L.J.; Wang, S.; Yin, G.J.; Guan, C.N. Fluid-structure interaction analysis of fluid pressure pulsation and structural vibration features in a vertical axial pump. *Adv. Mech. Eng.* **2019**, *11*. [CrossRef]
18. Yang, F.; Chang, P.C.; Jian, H.F.; Lv, Y.T.; Tang, F.P.; Jin, Y. Numerical Analysis of Unsteady Internal Flow Characteristics of Impeller-Guide Vane in a Vertical Axial Flow Pump Device. *Front. Energy. Res.* **2022**, *10*, 935888. [CrossRef]
19. Yang, F.; Li, Z.B.; Yuan, Y.; Liu, C.; Zhang, Y.Q.; Jin, Y. Numerical and Experimental Investigation of Internal Flow Characteristics and Pressure Fluctuation in Inlet Passage of Axial Flow Pump under Deflection Flow Conditions. *Energies* **2021**, *14*, 5245. [CrossRef]
20. Kan, N.Q.; Liu, Z.K.; Shi, G.T.; Liu, X.B. Effect of Tip Clearance on Helico-Axial Flow Pump Performance at Off-Design Case. *Processes* **2021**, *9*, 1653. [CrossRef]
21. Feng, J.J.; Luo, X.Q.; Guo, P.C.; Wu, G.K. Influence of tip clearance on pressure fluctuations in an axial flow pump. *J. Mech. Sci. Technol.* **2016**, *30*, 1603–1610. [CrossRef]
22. Li, D.L.; Zhang, N.; Jiang, J.X.; Gao, B.; Alubokin, A.A.; Zhou, W.J.; Shi, J.L. Numerical investigation on the unsteady vortical structure and pressure pulsations of a centrifugal pump with the vaned diffuser. *Int. J. Heat Fluid Flow* **2022**, *98*, 109050. [CrossRef]
23. Zhao, H.R.; Wang, F.J.; Wang, C.Y.; Chen, W.H.; Yao, Z.F.; Shi, X.Y.; Li, X.Q.; Zhong, Q. Study on the characteristics of horn-like vortices in an axial flow pump impeller under off-design conditions. *Eng. Appl. Comp. Fluid.* **2021**, *15*, 1613–1628. [CrossRef]
24. Zhang, W.P.; Tang, F.P.; Shi, L.J.; Hu, Q.J.; Zhou, Y. Effects of an Inlet Vortex on the Performance of an Axial-Flow Pump. *Energies* **2020**, *13*, 2854. [CrossRef]
25. Kan, K.; Zheng, Y.; Chen, Y.J.; Xie, Z.S.; Yang, G.; Yang, C.X. Numerical study on the internal flow characteristics of an axial-flow pump under stall conditions. *J. Mech. Sci. Technol.* **2018**, *32*, 4683–4695. [CrossRef]
26. Song, X.J.; Liu, C. Experimental investigation of floor-attached vortex effects on the pressure pulsation at the bottom of the axial flow pump sump. *Renew. Energ.* **2020**, *145*, 2327–2336. [CrossRef]
27. Wu, H.X.; Miorini, R.L.; Katz, J. Measurements of the tip leakage vortex structures and turbulence in the meridional plane of an axial water-jet pump. *Exp. Fluids.* **2011**, *50*, 989–1003. [CrossRef]
28. Spalart, P.R.; Jou, W.H.; Strelets, M.; Allmaras, S.R. Comments on the feasibility of LES for winds, and on a hybrid RANS/LES approach. In Proceedings of the Advances in DNS/LES, Ruston, LA, USA, 4–8 August 1997.
29. Spalart, P.R.; Deck, S.; Shur, M.L.; Squires, K.D.; Strelets, M.K.; Travin, A. A New Version of Detached-eddy Simulation, Resistant to Ambiguous Grid Densities. *Theor. Com. Fluid. Dyn.* **2006**, *20*, 181–195. [CrossRef]
30. Gritskevich, M.S.; Garbaruk, A.V.; Schütze, J.; Menter, F.R. Development of DDES and IDDES formulations for the k-ω shear stress transport model. *Flow. Turbul. Combust.* **2012**, *88*, 431–499. [CrossRef]
31. Wu, J.Z.; Ma, H.Y.; Zhou, M.D. *Vorticity and Vortex Dynamics*; Springer Science Business Media: Berlin, Germany, 2007.
32. Zhang, R.; Chen, H.X. Numerical analysis of cavitation within slanted axial-flow pump. *J. Hydrodyn.* **2013**, *25*, 663–672. [CrossRef]

33. Xie, X.; Li, Z.L.; Zhu, B.S.; Wang, H.; Zhang, W.W. Multi-objective optimization design of a centrifugal impeller by positioning splitters using GMDH, NSGA-III and entropy weight-TOPSIS. *J. Mech. Sci. Technol.* **2021**, *35*, 2021–2034. [CrossRef]
34. Tao, H.G.; Chen, H.X.; Xie, J.L.; Hu, Y.P. An alternative approach to quantifying fluid flow uniformity based on area-weighted average velocity and mass-weighted average velocity. *Energy. Build.* **2012**, *45*, 116–123. [CrossRef]